Retrieval of Sea Surface Range Velocities From Envisat ASAR Doppler Centroid Measurements

Morten Wergeland Hansen, Fabrice Collard, Knut-Frode Dagestad, Johnny A. Johannessen, Pierre Fabry, and Bertrand Chapron

***Abstract*—The processing steps and error corrections needed to retrieve estimates of sea surface range Doppler velocities from Envisat Advanced Synthetic Aperture Radar Wide Swath Medium resolution image products are presented. Retrieval accuracies based on examination of the corrected Doppler shift measurements are assessed. The root-mean-square errors of the Doppler shift after bias corrections are found to be 4.7 and 3.9 Hz in VV and HH polarizations, respectively. At 35° incidence angle, this corresponds to horizontal Doppler velocities of 23 and 19 cm/s.**

***Index Terms*—Doppler measurements, remote sensing, sea surface, synthetic aperture radar (SAR).**

Abbreviations and Acronyms

ASAR	Advanced SAR.
ATI	Along-track interferometry.
CLS	Collecte Localisation Satellites.
ESA	European Space Agency.
NRCS	Normalized radar cross section.
PRF	Pulse repetition frequency.
rms	Root mean square.
rmsd	rms deviation.
rmse	rms error.
SAR	Synthetic aperture radar.
SPECAN	Spectral analysis.
TR	Transmit/receive.
WSM	Wide Swath Medium resolution image.

Manuscript received October 29, 2010; revised January 26, 2011 and March 3, 2011; accepted May 1, 2011. Date of publication July 4, 2011; date of current version September 28, 2011. This work was supported in part by the Nansen Environmental and Remote Sensing Center, Bergen, Norway, through the Nansen Fellowship Fund, by the European Space Agency Synthetic Aperture Radar Ocean Wind-Wave and Currents project and Dragon-2 program under ESRIN Contract 18709/05/I-LG and 22494/09/I-LG, by the Changing Earth Science Network project IncuSAR, and by the Research Council of Norway under Contract 202311/V30.

M. W. Hansen and K.-F. Dagestad are with the Nansen Environmental and Remote Sensing Center, NO-5006 Bergen, Norway (e-mail: morten.hansen@nersc.no; knut-frode.dagestad@nersc.no).

F. Collard and P. Fabry are with the Division of Radar Applications, Collecte Localisation Satellites, 29280 Plouzané, France (e-mail: fcollard@cls.fr; pfabry@cls.fr).

J. A. Johannessen is with the Geophysical Institute, University of Bergen, NO-5020 Bergen, Norway, and also with the Nansen Environmental and Remote Sensing Center, 5006 Bergen, Norway (e-mail: johnny.johannessen@nersc.no).

B. Chapron is with the Institut Français de Recherche et Exploitation de la Mer, Laboratoire Océanographie Spatiale, Centre de Brest, 29280, Plouzané, France (e-mail: bertrand.chapron@ifremer.fr).

Digital Object Identifier 10.1109/TGRS.2011.2153864

I. Introduction

OVER THE ocean, the SAR instrument measures surface roughness linked to, e.g., wind, waves and currents, sea ice, and surface contaminants, including natural film and oil spill. In particular, current shear and convergence zones can affect the waves, resulting in wave steepening and enhanced SAR-detectable roughness changes. By this mechanism, detailed structures of mesoscale current dynamics have been observed and studied during the last decades [1]–[8]. Quantitative estimates of ocean currents have not been possible, except for very simple and idealized cases. However, within the last decade, considerable progress has been made in the development of two techniques that do permit a direct retrieval of line-of-sight (range) surface velocity fields from SAR data. One technique, called ATI, requires a second receiving antenna (or a split antenna) [9]–[14], while the single-antenna Doppler shift method enables estimates from conventional SAR raw data at a reduced spatial resolution [15]–[19]. The retrieved Doppler shift complements the NRCS measurements and may facilitate better quantitative interpretation of the relationship between the usual complex roughness pattern and upper ocean dynamic conditions.

Regarding the single-antenna Doppler shift method, a Doppler centroid anomaly is defined by

$$f_{\mathrm{Dca}} \equiv f_{\mathrm{Dc}} - f_{\mathrm{Dp}} \tag{1}$$

where f_{Dc} is the measured Doppler centroid defined as the radar return frequency shift at the antenna beam center and f_{Dp} is a predicted Doppler shift arising from the relative velocity V_{rel} of the satellite and rotating Earth. A geophysical Doppler shift relates to the Doppler centroid anomaly by

$$f_g = f_{\mathrm{Dca}} - f_{\mathrm{err}} \tag{2}$$

where f_{err} accounts for the estimation errors of both f_{Dc} and f_{Dp}. f_g should be zero for a surface at rest with respect to the Earth. For the dynamic sea surface, however, the geophysical Doppler shift relates to a spatial mean of the range component v_r of the velocity of the surface scattering elements, weighted by the local NRCS (σ_0) [11], [17] as

$$f_g = -k_e V_D/\pi = -\frac{k_e}{\pi}\frac{\overline{v_r\sigma_0}}{\overline{\sigma_0}} \tag{3}$$

where k_e is the electromagnetic wavenumber, V_D is defined as the range Doppler velocity, and the overbars characterize spatial averaging. The sign convention follows the one in [11] and [17], where a positive value of v_r corresponds to a target

which is receding from the radar. The local NRCS over water varies strongly in space and time due to effects such as the weighting of advancing and receding Bragg resonance waves (e.g., [10]), which depends strongly on the wind direction, specular reflection, and wave breaking, as well as tilt (e.g., [20]) and hydro- and aerodynamic modulations of the scattering elements (e.g., [21] and [22]). The interested reader is referred to the mentioned papers and [18], with references therein, for further discussion and quantification of these effects.

We are here concerned with the WSM product from the ASAR instrument aboard the ESA satellite Envisat ($k_e = 112\ \mathrm{m}^{-1}$ for a radar wavelength of 5.6 cm). The error term f_{err} contains some known biases which partly distort the retrieval accuracy of the Doppler centroid anomaly and need to be removed. Since

$$\frac{v_r}{V_{\mathrm{rel}}} \ll 1 \tag{4}$$

accurate estimation of these biases is here of great concern. Two independent effects are identified. These are related to gradients in surface backscatter along the azimuth direction and antenna mispointing and have only been briefly commented in previous literature [17]–[19].

In this paper, the intention is therefore to describe the processing steps needed to obtain f_g from ASAR WSM data and to assess the retrieval accuracies. We present the Doppler centroid and predicted Doppler shift data in Section II and describe the procedures for correction of the biases in Section III. The measurement accuracies are assessed in Section IV, and Section V contains the summary and concluding remarks.

II. ASAR WSM Doppler Centroid Anomalies

The ASAR WSM product is generated with the SPECAN algorithm [23] at 150-m resolution and about 420-km swath width. The fractional PRF part of the Doppler centroid is estimated using Madsen's method [24] and further refined using the look-power-balancing algorithm [25]. It is related to the frequency of the return signal at the center of the radar beam and determines the center frequency of the azimuth matched filter in the SAR processor. The Doppler centroid is essential in the processing of SAR data by affecting image focusing and noise and ambiguity levels in the processed image [23].

A grid of Doppler centroid frequencies has been included in Envisat ASAR WSM level-1b products since May 2007. The grid contains 100 pixels in the range direction, 20 for each of the 5 subswaths. The subswaths slightly overlap in slant range. The pixel spacing is regular in slant range within each subswath, corresponding to about 9 km in near range and 3.5 km in far range when projected to the surface. The pixel spacing in the azimuth direction is fixed at about 8 km.

The predicted geometrical Doppler shift is given by the relative velocity of the satellite and the rotating Earth according to a general formula demonstrated by [26]

$$f_{\mathrm{Dp}} = \frac{k_e V_{\mathrm{sc}}}{\pi} \sin\gamma \cos\alpha \times \left[1 - (\omega_e/\omega)(\epsilon \cos\beta \sin\Psi \tan\alpha + \cos\Psi)\right] \tag{5}$$

where

- V_{sc} is the magnitude of the spacecraft velocity along its orbital path;
- γ is the elevation angle of the radar beam;
- α is the angle between the range elevation plane and the spacecraft orbital plane (yaw);
- ω_e is the angular rate of the Earth's rotation;
- ω is the angular rate of the spacecraft;
- ϵ describes whether the radar is looking to the right $(+1)$ or left (-1) of the orbital velocity vector $(\epsilon_{\mathrm{ASAR}} = +1)$;
- β is the argument of latitude, defined as the angle between the ascending node (where the satellite crosses the equatorial plane in ascending pass configuration) and the spacecraft position in the orbital plane measured from the center of the Earth (this is not the same as the projected latitude onto the Earth's surface);
- Ψ is the inclination of the spacecraft orbital plane.

The geometry is illustrated in [26], and the satellite orbit is assumed circular [27]. The predicted Doppler shift, radar footprint geolocation parameters, and elevation angle are calculated with Envisat CFI mission analysis software[1] from ESA, using timing information and state vectors available in the ASAR WSM product. The CFI software uses a yaw steering law to maintain the Doppler shift within the baseband frequency $\pm\mathrm{PRF}/2$.

A schematic overview of the processing steps and error corrections needed to retrieve estimates of the geophysical Doppler shift, with symbols and expressions consistent with the content in Sections II and III, is shown in Fig. 1. The Doppler centroid and predicted Doppler shift, presented in this section, with resulting Doppler centroid anomalies f_{Dca} enter the loop in the upper rectangle.

III. Corrections of Nongeophysical Biases

The observed Doppler centroid (left) and predicted geometric Doppler shift (center) from an Envisat ASAR WSM scene (ascending pass) on September 14, 2010, acquired off the coast of South Africa are shown in Fig. 2. The Doppler centroid anomaly is shown in the right panel. Some artifacts are, however, observed. A large variability of f_{Dca} is seen, also over land where the geophysical Doppler shift is expected to be zero. Much of this variability is due to backscatter gradients along the azimuth direction within the estimation area of the Doppler centroid pixels. Discontinuities aligned in the azimuth direction correspond to a bias introduced by electronic mispointing of the SAR antenna. In addition, inaccuracies exist in the theoretical radar beam pointing angle caused by errors in satellite orbit and attitude parameters [see (5)]. In combination with electronic mispointing, these cause an rms offset, from zero, of about 17.1 Hz over land in this image.

The error term from (2) can thus be partitioned as

$$f_{\mathrm{err}} = f_{\sigma_0} + f_{\mathrm{pe}} + f_{\Delta} \tag{6}$$

[1] http://eop-cfi.esa.int/CFI/cfi_software.html

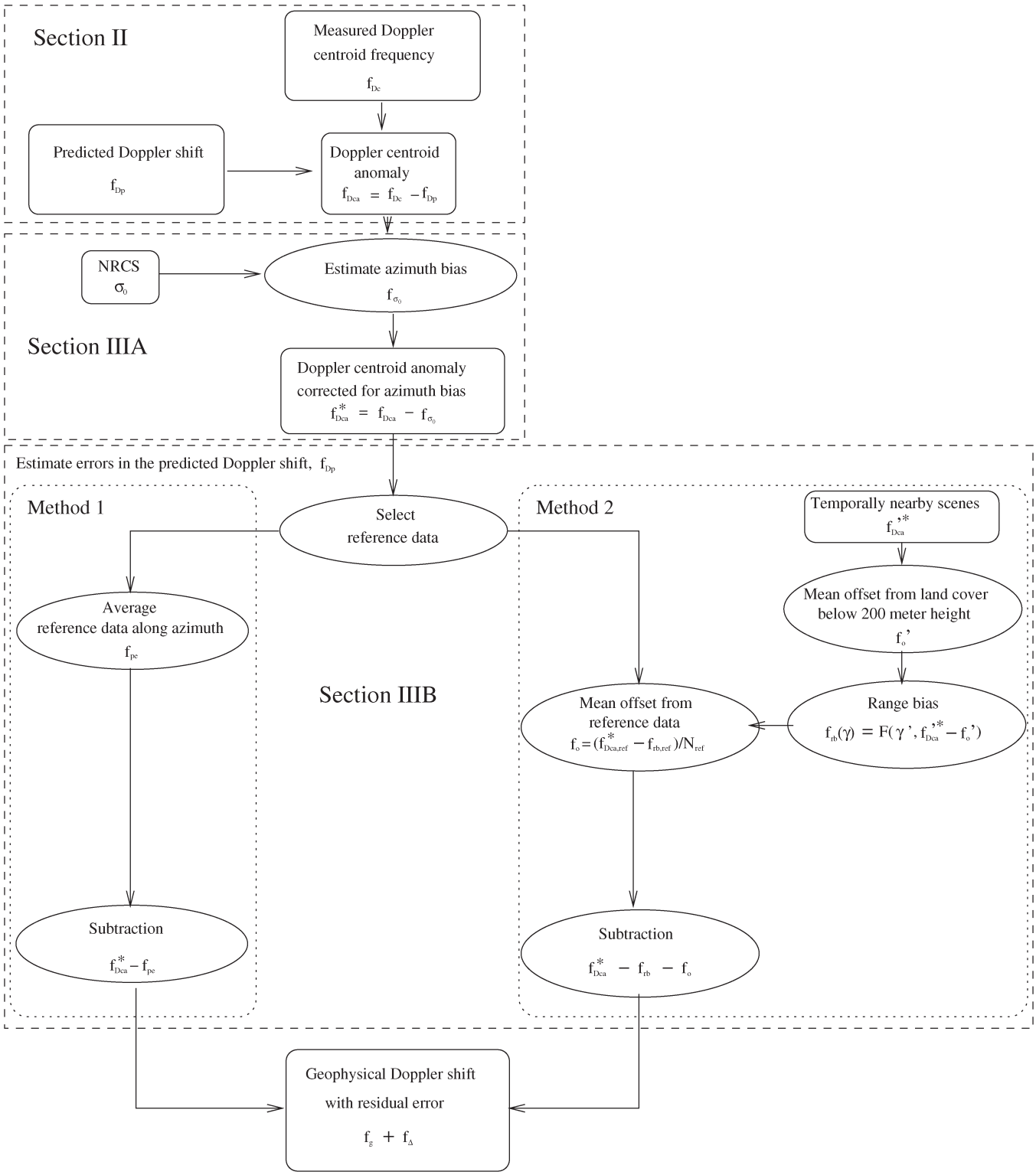

Fig. 1. Schematic overview of the processing steps and error corrections needed to retrieve estimates of the geophysical Doppler shift f_g. The symbols and various expressions will be further explained in Sections II and III.

where f_{σ_0} is a Doppler centroid shift caused by NRCS gradients along azimuth, f_{pe} is an error in the predicted Doppler shift caused by the use of wrong radar beam pointing angles, and f_Δ is the residual error. These biases and their corrections are further described in the following sections, which relate to the lower dashed box in Fig. 1.

A. Azimuthal Variation of NRCS

In general, the SAR azimuth power spectrum exhibits a pattern similar to the antenna power pattern. The Doppler centroid can therefore be estimated by searching for the maximum of this spectrum. However, in cases with large backscatter gradients within the physical (azimuth) beamwidth of the SAR

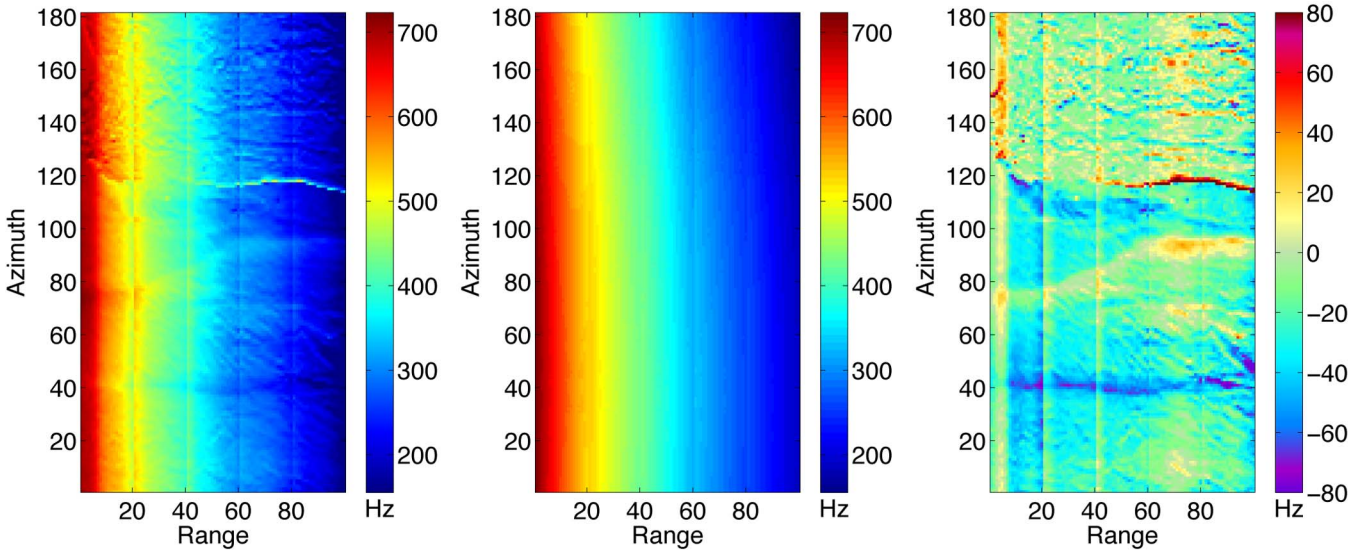

Fig. 2. Left panel shows the Doppler centroid (f_{Dc}) estimated from an Envisat ASAR WSM scene acquired off the coast of South Africa on September 14, 2010, at 21:15 UTC. The polarization is VV, and the pass is ascending, with sensor looking toward the right. The Doppler grid pixel numbers along the range and azimuth directions are given on the axes. The center panel shows the corresponding predicted Doppler shift (f_{Dp}), and the right panel shows the Doppler centroid anomaly (f_{Dca}). Separation between land (to the north) and water is seen around azimuth pixel number 120, and discontinuities visible as stripes along the azimuth direction indicate the borders between the 5 subswaths of 20 pixels each.

antenna, the accuracy of this technique is reduced [28]. Accordingly, any region with relatively strong or weak intensity away from the center of the radar beam (e.g., at land–water boundaries) can bias the Doppler centroid estimate. Although reduced with Madsen's method (which operates in the time domain) [24] and the look-power-balancing algorithm [25], this bias is still present in the Doppler centroid from the ASAR WSM product over both ocean and land.

The right view in Fig. 3 shows the NRCS at original resolution (150 × 150 m) within the area covered by a single Doppler centroid pixel from the same scene as in Fig. 2. Higher relative NRCS over land in the upper part than over ocean in the lower part results in a shift of the Doppler centroid estimate toward higher frequencies (forward in azimuth time). A correction of this shift is necessary and is here performed by finding a relation between the gradients of backscatter and Doppler centroid anomalies f_{Dca}, along azimuth from succeeding pixels over land. The use of f_{Dca} minimizes the influence from the variation of f_{Dc} along the satellite orbit, which is caused by changing relative velocities between the satellite and Earth.

A measure of the NRCS gradient within a Doppler pixel is found by calculating

$$\Delta\sigma_{0,y} = \sum_{l=1}^{N_y}\left(\frac{2l}{N_y} - 1\right)\sum_{k=1}^{N_x}\sigma_0(k,l) \tag{7}$$

where k and l are the pixel numbers of NRCS within the Doppler centroid estimate in range and azimuth directions, with a total number of (N_x, N_y) pixels. The sum along range represents the total backscatter within the Doppler centroid estimation area at given azimuth l. A weighting is then performed, such that a theoretical surface with constant NRCS $(d\sigma_0/dy = 0)$ would exhibit a linear variation from $-\sum_{k=1}^{N_x}\sigma_0(k,1)$ to $\sum_{k=1}^{N_x}\sigma_0(k,N_y)$. The total sum should therefore be zero for this theoretical surface. With $(d\sigma_0/dy) \propto \Delta\sigma_{0,y}$, any deviation

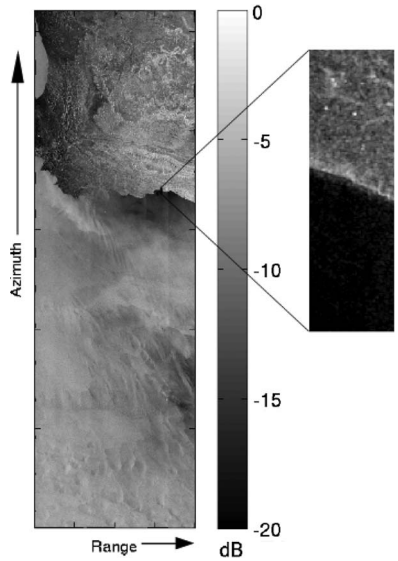

Fig. 3. NRCS of the ASAR WSM image over the Agulhas region on September 14, 2010. The right view is the NRCS at original resolution (150 × 150 m) within a single Doppler centroid pixel.

from zero represents the NRCS gradient within the Doppler centroid pixel. Furthermore, a variation of $\Delta\sigma_{0,y}$ along azimuth (in the reduced resolution Doppler centroid grid) will cause a related variation of the biased Doppler centroid values. By discrete convolution with a 1×3 $(range \times azimuth)$ kernel $g = \begin{pmatrix} -1 \\ 0 \\ 1 \end{pmatrix}$, estimates of $\partial f_{Dca}/\partial y$ and $\partial(\Delta\sigma_{0,y})/\partial y$ are calculated and shown in Fig. 4. This figure demonstrates a linear relation

$$\frac{\partial f_{\mathrm{Dca}}}{\partial y} = c\frac{\partial(\Delta\sigma_{0,y})}{\partial y} + A \tag{8}$$

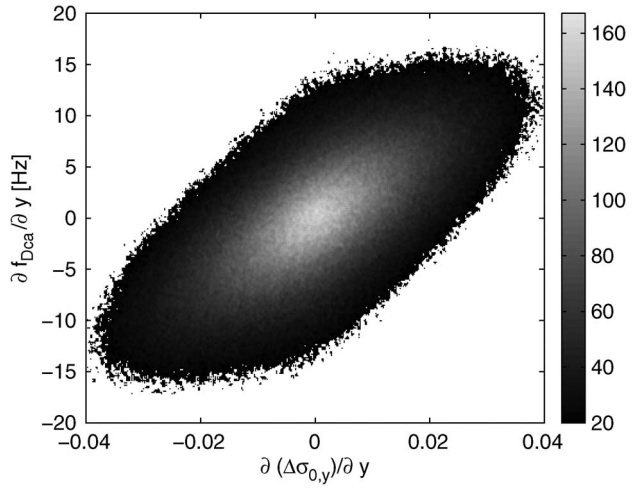

Fig. 4. Two-dimensional histogram of Doppler centroid anomaly gradients along azimuth $\partial f_{\mathrm{Dca}}/\partial y$ versus the gradients of backscatter variation $\partial(\Delta\sigma_{0,y})/\partial y$ calculated over land cover from 1610 scenes in VV polarization.

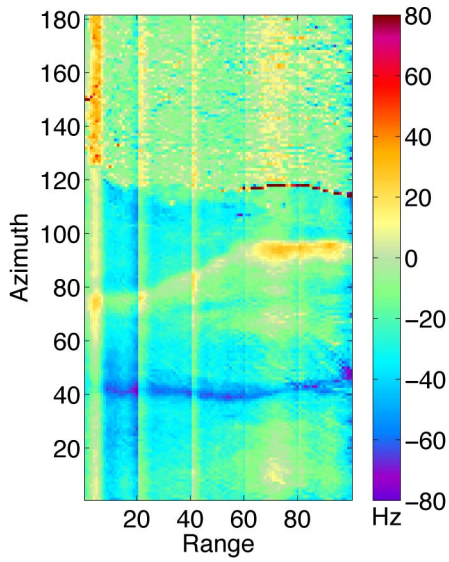

Fig. 5. Doppler centroid anomaly f^*_{Dca} after correction of the azimuth bias (see right panel of Fig. 2).

where the constants c and A can be found by a polynomial fit to the observations (note that we are now operating on the full Doppler centroid grid, whereas (7) operates on the NRCS within one single Doppler centroid estimate). By integration, this gives

$$f_{\mathrm{Dca}}(y) = c\Delta\sigma_{0,y}(y) + Ay + B \tag{9}$$

in which case B is assumed to result from processes not related to azimuthal variation of the NRCS. The constant A is here found to be zero, and the error in the Doppler centroid frequency caused by azimuthal variations of NRCS is therefore given by $f_{\sigma_0} = c\Delta\sigma_{0,y}$. The magnitude of c depends on polarization and incidence angle. It also varies with time and must therefore be found by using other acquisitions temporally nearby the scene under consideration. The Doppler centroid anomaly (see Fig. 1) corrected for this *azimuth bias* is, in the following, marked by an asterisk $(*)$, i.e.,

$$f^*_{\mathrm{Dca}} = f_{\mathrm{Dca}} - f_{\sigma_0}. \tag{10}$$

Fig. 5 shows the corrected Doppler centroid anomaly f^*_{Dca} for the scene shown in Fig. 2. We see that the variability of f^*_{Dca} is less than that of f_{Dca} (Fig. 2, right), and the rms offset over land is reduced to 16.0 Hz. The remaining errors are still evident and are discussed in the following sections.

B. Errors in the Predicted Doppler Shift

A departure of the radar beam pointing angle from the theoretical pointing angle used to calculate the predicted Doppler shift will cause an offset between f_{Dp} and f_{Dc}. A 0.01° pointing error in yaw (rotation about the vertical axis) would, for instance, give an error in f_{Dp} of about 14 Hz at $\gamma = 20°$ and about 27 Hz at $\gamma = 40°$ [see (5)]. Such departures may be caused by both electronic mispointing and wrong satellite orbit and attitude parameters. A correct partitioning of these contributions is challenging, although two main effects seem apparent. A variation along range is related to the enhanced/reduced frequencies aligned in the azimuth direction shown in Figs. 2 and 5. This is most clearly seen over land in the first image swath, where the Doppler centroid anomaly is first seen at about 30 to 40 Hz approximately between range pixel numbers 1 and 7, before it is reduced to between 0 and −10 Hz approximately between range pixel numbers 8 and 20. We will refer to this as the *range bias*. In addition to this, there is an offset from the expected mean zero Doppler shift over land. The antenna pointing error [see (6)] may therefore be partitioned as

$$f_{\mathrm{pe}} = f_{\mathrm{rb}} + f_o \tag{11}$$

where f_{rb} is the range bias and f_o is the mean offset from zero over land.

The antenna pattern defines the azimuth direction of maximum backscattered radiation and is not constant along radar beam elevation angles γ. This direction should ideally be aligned with the direction of zero Doppler shift but is slightly shifted due to imperfect relative functionality of the antenna TR modules. This cannot currently be modeled to the needed accuracy. It is thus observed as slight shifts of antenna boresights (along yaw) within each subswath and appears to be the main source of the range bias which, consequently, can be expressed as a function of elevation angle: $f_{\mathrm{rb}} = f_{\mathrm{rb}}(\gamma)$.

Fig. 6 shows the range bias (right), calculated from $f^*_{\mathrm{Dca}} - f_o$, for the nearest subswath (range index of 1–20) of one acquisition over the Amazon rain forest (left) and one over the Greenland ice sheet (center), both in HH polarization. f_o is here estimated by averaging the values of f^*_{Dca} within each subswath. With a perfect antenna model for the Doppler shift prediction, the range bias should be zero (disregarding the residual error term f_Δ). However, it is here seen to vary with elevation angle $(f_{\mathrm{rb}} = f_{\mathrm{rb}}(\gamma))$. The shift of up to 1° in the elevation angle of Amazon and Greenland data is caused by the difference in mean topographic height between the imaged areas (2540 versus 140 m above sea level for the given examples). As a consequence, it is possible to use Doppler centroid

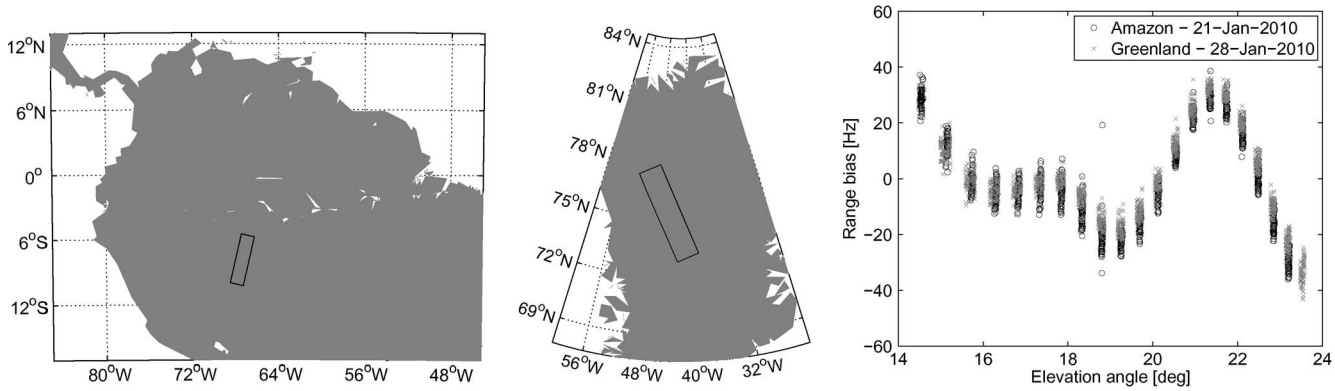

Fig. 6. Locations of two example scenes (first subswath) in HH polarization over (left) the Amazon rain forest and (center) the Greenland ice sheet from January 21 and 28, 2010, respectively. The right panel shows the range bias $f^*_{\mathrm{Dca}} - f_o$ in the first subswath plotted against elevation angles γ.

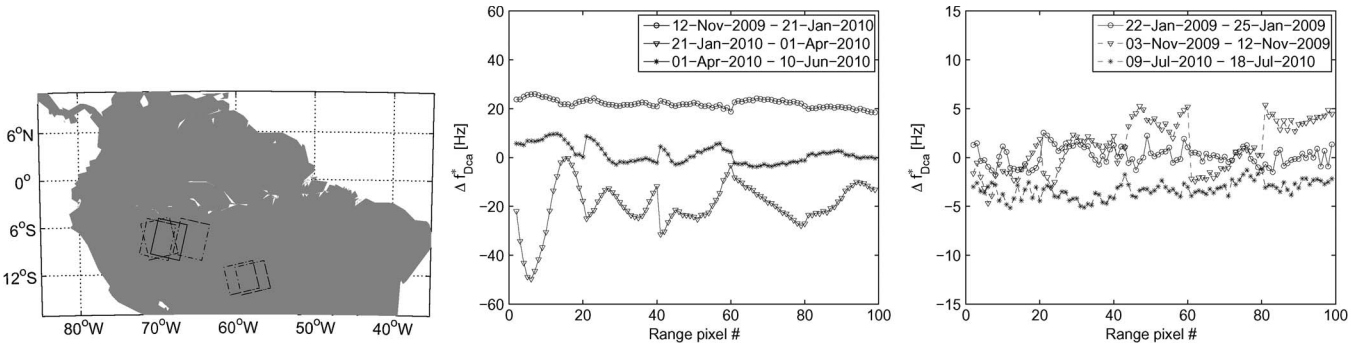

Fig. 7. Coverage of repeated image acquisitions over (left) the Amazon used for stability analysis. The center panel shows the Doppler centroid anomalies f^*_{Dca} (in hertz) after averaging along azimuth. The scenes are overlapping and are acquired in descending pass configuration (continuous rectangle in the left panel) covering the same area at 70-day separation (two repeat track periods). The right panel shows differences between (o) ascending, ($\bigtriangledown$) descending and ascending, and ($*$) descending pass for scenes at three- and nine-day separations. These scenes do not cover the exact same areas (dashed–dotted rectangles in the left panel). Note that the scales of the y-axes in the center and right panels are different.

anomaly data covering land at any location to estimate $f_{\mathrm{rb}}(\gamma)$ by a curve fit to the measured data $(\gamma, f_{\mathrm{rb}})$. The values of f_{rb} at $\gamma(h = 0)$, where h is the topographic height, can then be used to find the range bias over the ocean.

For checking the correction ability, we now form bias differences of one scene with another scene of some temporal separation. The left panel of Fig. 7 shows the coverage of repeated ASAR WSM scenes acquired over the Amazon in 2009 and 2010. The scenes are selected because of the uniform backscatter from this area, hence allowing f_{pe} to be examined with minimum distortion from the azimuth bias. In the center panel of Fig. 7, the Doppler centroid anomaly f^*_{Dca} is compared between three pairs of scenes acquired at 70-day separation. This corresponds to two repeat track periods. Hence, the surface geometry and the satellite attitude angles are potentially unchanged. Large variations are seen both as constant offsets within each subswath and also as relative variations along range. These are mainly caused by reprogramming of the excitation coefficients of ASAR TR modules and the resulting effect on electronic mispointing (the antenna pattern) in March [29]. The right panel of Fig. 7 shows differences in three pairs of scenes at three- and nine-day separations. Here, both the offsets and the range relative variations are much smaller (within 5 Hz). Differences are here caused by changes in the antenna pattern related to minor failures and/or drift of the TR modules, as well as errors in satellite position and attitude used to predict the Doppler shift.

TABLE I
COMPARISONS OF $f^*_{\mathrm{Dca}} - f_o$ OVER THE AMAZON FOREST

Date of first acquisition	Temporal separation (days)	rmsd [Hz]	Polarization	Remark
12-Nov-2009	70	1.1	H/H	–
21-Jan-2010	70	9.2	H/H	Antenna reset in March
01-Apr-2010	70	2.6	H/H	–
22-Jan-2009	3	1.3	V/V	–
03-Nov-2009	9	1.7	H/H	–
09-Jul-2010	9	1.0	H/H	–

A removal of the mean offset over land in each subswath is a simple first-order correction to remove Doppler shift prediction errors from the Doppler centroid anomaly f^*_{Dca}. Table I thus presents rmsds from the comparisons in Fig. 7 after subtracting the mean offset in each subswath of each scene. These numbers represent a measure of the temporal stability of the antenna pattern, and we see that, within short time periods (e.g., three and nine days), this pattern appears stable within 1–2 Hz. Within longer periods, however, the risk of significant variations of the antenna pattern increases. Between April 1 and June 10, 2010, the rmsd reaches 2.6 Hz, and with occasional antenna resets

(e.g., March 2010), the changes are even larger. Since the range bias is related to the antenna pattern, any data to estimate this bias in a given scene should therefore be acquired as close as possible in time. The antenna pattern should also be monitored for any sudden changes due to antenna resets or other electronic failures.

Two methods (see Fig. 1) have been developed to estimate $f_{\rm pe}$. Common to these is the use of reference data for which the geophysical Doppler shift is assumed zero, such as over land. However, very often, some of the subswaths within a SAR scene do not cover land. It is then possible to utilize ocean data corrected for the wind-induced Doppler shift f_w as an approximate zero level. In [17] and [30], it was found that wind-induced short-period waves contribute the most to the Doppler anomaly signal in areas of insignificant surface current. An empirical model, called C-band Doppler (CDOP) shift model, has been developed to provide the wind-dependent Doppler shift f_w from the wind speed and direction with respect to the antenna look direction [31], [32]. This model is thus the counterpart of C-band MODel function [33], which relates NRCS to wind. If there is insufficient land cover within a scene, an approximation to the zero geophysical Doppler shift reference level can thus be found by subtracting the modeled wind contribution from the Doppler centroid anomaly over ocean. This has the consequence that observations are biased toward wind model and any residual surface current. The CDOP model is presently only available for VV polarization, and the HH data presented here are therefore corrected strictly by the use of land cover.

In the following, the two approaches computing $f_{\rm pe}$ directly [method (i)] or via $f_{\rm rb}$ and f_o [method (ii)] from land cover and/or modified ocean cover are presented (see Fig. 1). Since $f^*_{\rm Dca} = f^*_{\rm Dca}(\gamma)$ and $\gamma = \gamma(h)$, we introduce a general requirement not to use land above 200-m height above sea level for the estimation of $f_{\rm pe}$ with method (i) and f_o with method (ii). The 200-m limit is selected as a compromise to get accurate Doppler shift estimates from acquisitions covering land areas at low height and to obtain a statistically significant amount of data optimally corrected by land reference. As such, the choice of height is therefore not definitive and could be changed for different acquisitions, depending mainly on the coverage. For the purpose of the accuracy assessment in this paper, however, it is better to keep the height limit consistent. Moreover, if there is insufficient reference data over land, CDOP is used to correct $f^*_{\rm Dca}$ over the ocean for the wind contribution.

Method (i): The simplest estimate of the Doppler shift prediction error (lower left rectangle of Fig. 1) is an average of zero level reference data along azimuth (constant range and elevation angle)

$$f_{\rm pe}(k) = \frac{1}{N_y}\sum_{l=1}^{N_y} f^*_{\rm Dca}(k,l) \tag{12}$$

where k denotes the range indices in the set $\{1, 2, \ldots, 100\}$, l denotes the azimuth indices of reference pixels, and N_y is the number of reference pixels along azimuth. Reference data are therefore required in every azimuth line. Combining (2), (6), and (10), the geophysical Doppler shift can now be expressed as

$$f_g = f^*_{\rm Dca} - f_{\rm pe} - f_\Delta \tag{13}$$

where f_Δ is the residual error.

Method (ii): An alternative method to remove errors in the predicted Doppler shift is represented by the lower right rectangle in Fig. 1. This method uses reference data from scenes within a given time interval (e.g., ± 3 days) before and/or after the acquisition. This provides more land cover and thus less use of ocean cover corrected for wind contribution. The selected scenes must first be corrected for the mean offset f'_o to provide a basis for the calculation of range bias dependence on elevation angle. This is here performed strictly by the use of reference data from land cover below 200-m height above sea level. If there is insufficient reference data in any of the scenes, they are discarded. Since the number of pixels over land can vary between azimuth lines, the mean offset is calculated by averaging first along azimuth, then along range in each subswath of each nearby scene

$$f'_o = \frac{1}{N_x}\sum_{k=1}^{N_x}\frac{1}{N_y}\sum_{l=1}^{N_y} f'^*_{\rm Dca}(k,l) \tag{14}$$

where $N_x = 20$ is the number of azimuth lines in every subswath and N_y is the number of reference pixels along azimuth. Primed parameters denote that this yields nearby scenes, only used for the estimation of $f_{\rm rb}(\gamma)$. By curve fitting, the offset corrected data are now used to give the range bias as a function of elevation angle

$$f_{\rm rb}(\gamma) = F\left(\gamma', f'^*_{\rm Dca} - f'_o\right) \tag{15}$$

and the mean offset in the present scene is found by averaging

$$f_o = \frac{1}{N}\sum_{n=1}^{N}\left[f^*_{\rm Dca}(n) - f_{\rm rb}\left(\gamma\left(h(n)\right)\right)\right] \tag{16}$$

where n denotes the indices of reference pixels and N is the total number of reference pixels in each subswath. Since the offset estimate in method (ii) is an average of all available reference data, fewer pixels are needed than with method (i). Compared to method (i), this method therefore more often succeeds by using reference data strictly from land cover. Combining (11) and (13), the geophysical Doppler shift (lower right part of Fig. 1) is now expressed as

$$f_g = f^*_{\rm Dca} - f_{\rm rb} - f_o - f_\Delta. \tag{17}$$

Fig. 8 shows the geophysical Doppler shift with residual error term f_Δ after correction of the azimuth bias and prediction error, using method (i). In this case, the land cover below 200-m height above sea level was insufficient, and ocean data corrected for wind contribution were used. With method (ii), however, subswaths 1 and 2 covered sufficient land (not shown). The

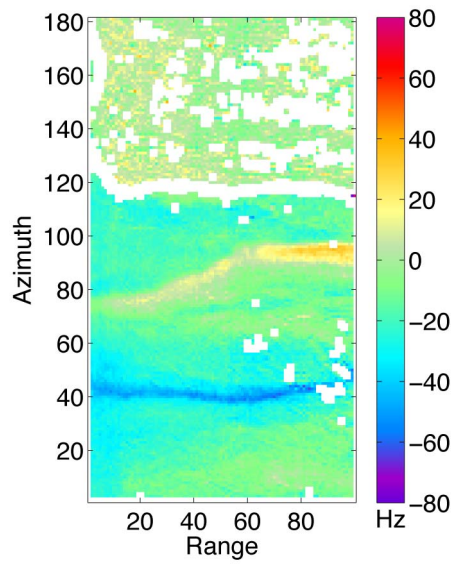

Fig. 8. Doppler anomaly grid from Fig. 5, after correction of errors in the predicted Doppler shift using method (i). The white regions are data flagged invalid. Positive (negative) f_{Dca} means motion toward (away from) the radar antenna.

white regions in Fig. 8 are flagged invalid either because of proximity to land, strong azimuthal NRCS gradients, or NRCS below -20 dB, which makes the interpretation of f_g highly uncertain.

The geophysical Doppler shift with residual error f_Δ shown in Fig. 8 is much smoother and more coherent than the starting point shown in the right panel of Fig. 2, and the rms offset over land is here 6.5 Hz. Over the ocean, we find bands of range-directed positive and negative frequencies corresponding to motions toward and away from the sensor. These bands correspond to the Agulhas current and the Agulhas return current with velocities reaching up to 2.5 and 1.5 m/s, respectively. The sea surface range Doppler velocity V_D with residual error V_Δ can now be calculated by

$$V_D + V_\Delta = -\frac{\pi(f_g + f_\Delta)}{k_e}. \tag{18}$$

Both wind-generated waves and current contribute to this quantity. However, separation of V_D into contributions from these parameters is out of the scope of this paper but is discussed in other papers referred to in Section I.

IV. Retrieval Accuracy

Since the geophysical Doppler shift should be zero over land, the deviation of $f_g + f_\Delta$ from this zero is an estimate of the residual error f_Δ. In this section, we examine this deviation expressed by rmses over land below 200-m height. A total of 866 and 863 acquisitions in VV and HH polarizations over the Amazon forest and other areas around the globe are analyzed. The number of corrected scenes using the different methods and the corresponding rmses, expressed as frequencies (f_Δ) and range Doppler velocities ($V_\Delta = |\pi f_\Delta / k_e|$), are summarized in Tables II and III. Note that, due to varying land cover between image subswaths, one scene can be corrected with more than one method, or it may have been disregarded. This causes a difference between the number of analyzed files (866 and 863 for VV and HH, respectively) and the sum of the number of files in the third columns of Tables II and III. The fourth table columns provide the total number of pixels which was used to estimate the rmses. To avoid outliers, pixels deviating from the mean by more than three times the standard deviation have been removed prior to rmse calculation. In VV polarization, separate estimates are also provided for scenes which were corrected from ocean data corrected for wind contribution to find the zero level of f_g. These corrections were only performed when there was insufficient land cover in the scene, and consequently, the wind corrections are more abundant with method (i). It is also seen that the number of (corrected) scenes in HH polarization is very low compared to the number analyzed (863). The HH data used in this study cover mainly latitudes above 65° north, with a large abundance of scenes over the Fram Strait between Greenland and Svalbard. Unless the scenes are very long, the land cover in this data is usually over Greenland at high altitudes (> 200 m). The estimation of f_{pe} with method (i) and f_o with method (ii) is therefore not performed for a large number of scenes. Corrections of ocean cover with a CDOP model for HH polarization will, however, provide more corrected data in the future.

As expected, the rmse over land is least for scenes over the Amazon forest where the error term f_{σ_0} is the smallest. The rmse over other land areas is about 1.5–2 Hz larger than that over this area. For VV polarization, the overall rmse is 4.7 Hz with method (i) and is 4.9 Hz with method (ii). When the zero Doppler shift reference level is estimated over ocean, the

TABLE II
rmses Over Land—VV Polarization

Range Bias Correction	Area (s)	# of files	# of pixels [10^3]	rmse f_Δ [Hz]	rmse V_Δ [cm/s]
(i)	Amazon	38	136	2.6	7
(i)	All available	325	909	4.7	13
(i)*	All available	674	293	5.3	15
(ii)	Amazon	41	135	2.6	7
(ii)	All available	642	1204	4.9	14
(ii)*	All available	416	8	7.5	21

* Poor land coverage. Corrected using additional data covering the ocean, subtracted by wind Doppler estimates.

TABLE III
rmses Over Land—HH Polarization

Range Bias Correction	Area (s)	# of files	# of pixels [10^3]	rmse f_Δ [Hz]	rmse V_Δ [cm/s]
(i)	Amazon	34	119	2.5	7
(i)	All available	149	701	3.9	11
(ii)	Amazon	33	117	2.5	7
(ii)	All available	264	749	4.0	11

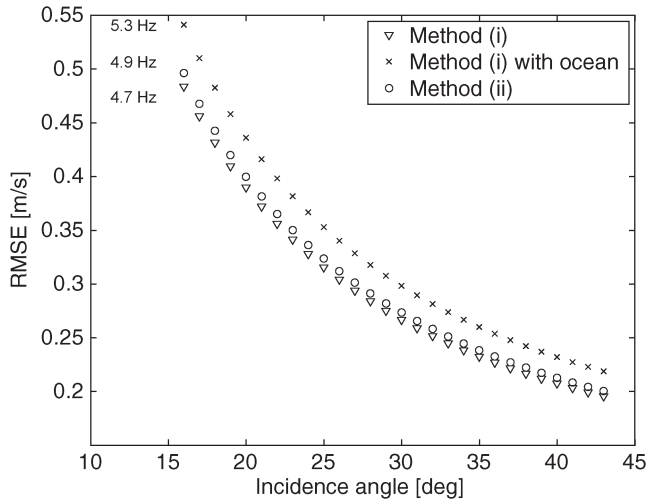

Fig. 9. Accuracies of range Doppler velocities in VV polarization estimated by methods (i) and (ii), projected to the horizontal plane. Corresponding rmses [in hertz] are given to the left of the graphs for each method.

corresponding numbers are 5.3 and 7.5 Hz. In this case, there is very poor land coverage, particularly when method (ii) has been applied. The statistical significance of the accuracy results for this data is therefore lower than that corrected purely by the use of land. For HH polarization, the rmses are 3.9 and 4.0 Hz for methods (i) and (ii), respectively. This may indicate that HH is more attractive for the use of the SAR Doppler shift method. However, since scenes in HH and VV are generally acquired at different latitudes and due to different scattering mechanisms over land and ocean, we will not draw any conclusions on this difference. Based on these findings, we therefore suggest the following order of priority for the correction of errors in the predicted Doppler shift:

1) Method (i) using land cover;
2) Method (ii) using land cover;
3) Method (i) using wind correction over the ocean;
4) Method (ii) using wind correction over the ocean.

The 200-m height limit for land correction is a rather strict requirement which limits the data amount properly corrected for these biases. Method (i) therefore often fails unless wind correction is applied. With method (ii), however, certain areas with poor land coverage, for instance the northern and central North Sea and the Norwegian Sea, may still be well corrected for the errors in predicted Doppler shifts.

Fig. 9 shows the rmses of range Doppler velocities (VV polarization) calculated with methods (i) and (ii), projected to the horizontal ($V_{\Delta,\mathrm{horizontal}} = V_\Delta / \sin\theta$), and plotted against incidence angle θ. To reach a surface range Doppler velocity accuracy of 30 cm/s or less along the horizontal, methods (i) and (ii) using reference data over land therefore require the use of incidence angle above 26° and 27°, respectively. The corresponding limit for scenes corrected with reference data over the ocean is 30° [method (i)]. Note that the comparison between range surface current calculated from f_{Dca} [method (i)] and surface Lagrangian drifter velocities reported by [19] also provided rmsds between 20 and 35 cm/s for incidence angles above 30°. This is in consistence with the results shown in Fig. 9.

V. Summary and Conclusion

This paper has described the processing steps needed to retrieve estimates of a geophysical Doppler shift from Envisat ASAR WSM level-1b products. The basic assumption is, in this respect, that the subtraction of geometrically predicted Doppler shifts from measured Doppler centroid frequencies can be performed to retrieve a Doppler centroid anomaly which can be related to sea surface motion. This method has been demonstrated by other authors with promising results. However, the Doppler centroid anomaly contains some known biases which partly distort the retrieval accuracy of the Doppler centroid anomaly, and need to be removed. In this paper, we have looked at the processing scheme in closer detail with specific attention to error corrections (see Fig. 1). Following the retrieval of a Doppler centroid anomaly, the processing scheme is shortly summarized as a correction of biases caused by variation of NRCS along azimuth and a correction of biases caused by Doppler shift prediction errors.

Two methods for estimating the biases caused by Doppler shift prediction errors have been presented. Both methods use reference data for which the geophysical Doppler shift is assumed zero. Method (i) takes data from the present scene, while method (ii) also uses data from scenes nearby in time (± 3 days). The accuracy estimates in Section IV showed that using land cover with method (i) is preferred. However, for scenes with insufficient land cover, the second method or ocean data corrected for the wind contribution to the Doppler shift are good substitutes.

The rmse of VV-polarized data corrected by method (i) with land reference was found to be 4.7 Hz. This corresponds to a horizontal Doppler velocity of 23 cm/s at 35° incidence angle. In HH polarization, the corresponding number is 3.9 Hz, which translates to a horizontal velocity of 19 cm/s at the same incidence angle. Since scenes in HH and VV are generally acquired at different latitudes (HH typically above 65° north) and due to different scattering mechanisms over land and ocean, we do not draw any conclusions on this slightly better performance for HH.

The use of the single-antenna Doppler shift method for retrieving ocean range surface current velocity is a topic of great interest and is discussed in detail in [18] and [19]. In this respect, we calculate the rmses of surface range Doppler velocities projected to the horizontal in Section IV. It is shown that a horizontal accuracy of 30 cm/s or less requires the use of incidence angles above 26° and 27° with methods (i) and (ii) (land reference), respectively. The geophysical Doppler shift from SAR also provides an additional source of wind information to reduce the wind direction ambiguity in the inversion of high-resolution wind fields from SAR imagery, as discussed in [17], [32], and [34]. ASAR WSM Doppler shift products are routinely processed [method (i)] in near real time at CLS from the Envisat rolling archive and are freely available for download at the Soprano ocean product Web site of CLS.[2]

Envisat ASAR was not designed to provide the Doppler centroid as a source of geophysical information. In 2013, ESA will

[2]http://soprano.cls.fr

launch a new C-band SAR mission with the Sentinel-1 satellite. The Doppler velocity will here be provided as an official product with higher accuracy and improved error correction. This will be accomplished by improving the accuracy of the Doppler centroid estimate and by the use of a precise antenna model to estimate electronic mispointing and related Doppler shift variation with elevation angle within each subswath. The potential for applications of the single-antenna Doppler shift is therefore likely to improve in the near future.

ACKNOWLEDGMENT

The authors would like to thank three anonymous reviewers for the valuable comments and feedback.

REFERENCES

[1] L. L. Fu and B. Holt, "Some examples of detection of oceanic mesoscale eddies by the SEASAT synthetic-aperture radar," *J. Geophys. Res.—Oceans Atmos.*, vol. 88, no. C3, pp. 1844–1852, Feb. 1983.

[2] W. Alpers and I. Hennings, "A theory of the imaging mechanism of underwater bottom topography by real and synthetic aperture radar," *J. Geophys. Res.—Oceans*, vol. 89, no. C6, pp. 10 529–10 546, Nov. 1984.

[3] D. R. Lyzenga and J. R. Bennett, "Full-spectrum modeling of synthetic aperture radar internal wave signatures," *J. Geophys. Res.—Oceans*, vol. 93, no. C10, pp. 12 345–12 354, Oct. 15, 1988.

[4] G. O. Marmorino, R. W. Jansen, G. R. Valenzuela, C. L. Trump, J. S. Lee, and J. A. C. Kaiser, "Gulf-stream surface convergence imaged by synthetic-aperture radar," *J. Geophys. Res.—Oceans*, vol. 99, no. C9, pp. 18 315–18 328, Sep. 15, 1994.

[5] C. S. Nilsson and P. C. Tildesley, "Imaging of oceanic features by ERS-1 synthetic-aperture radar," *J. Geophys. Res.—Oceans*, vol. 100, no. C1, pp. 953–967, Jan. 15, 1995.

[6] J. A. Johannessen, R. A. Shuchman, G. Digranes, D. R. Lyzenga, C. Wackerman, O. M. Johannessen, and P. W. Vachon, "Coastal ocean fronts and eddies imaged with ERS 1 synthetic aperture radar," *J. Geophys. Res.—Oceans*, vol. 101, no. C3, pp. 6651–6667, Mar. 15, 1996.

[7] R. Romeiser and W. Alpers, "An improved composite surface model for the radar backscattering cross section of the ocean surface .2. Model response to surface roughness variations and the radar imaging of underwater bottom topography," *J. Geophys. Res.—Oceans*, vol. 102, no. C11, pp. 25 251–25 267, Nov. 15, 1997.

[8] J. A. Johannessen, V. Kudryavtsev, D. Akimov, T. Eldevik, N. Winther, and B. Chapron, "On radar imaging of current features: 2. mesoscale eddy and current front detection," *J. Geophys. Res.—Oceans*, vol. 110, no. C7, p. C07017, Jul. 22, 2005.

[9] R. M. Goldstein and H. A. Zebker, "Interferometric radar measurement of ocean surface currents," *Nature*, vol. 328, no. 6132, pp. 707–709, Aug. 20, 1987.

[10] D. R. Thompson and J. R. Jensen, "Synthetic-aperture radar interferometry applied to ship-generated internal waves in the 1989 Loch Linnhe experiment," *J. Geophys. Res.—Oceans*, vol. 98, no. C6, pp. 10 259–10 269, Jun. 15, 1993.

[11] R. Romeiser and D. R. Thompson, "Numerical study on the along-track interferometric radar imaging mechanism of oceanic surface currents," *IEEE Trans. Geosci. Remote Sens.*, vol. 38, pt. 2, no. 1, pp. 446–458, Jan. 2000.

[12] R. Romeiser, H. Breit, M. Eineder, H. Runge, P. Flament, K. de Jong, and J. Vogelzang, "Current measurements by SAR along-track interferometry from a space shuttle," *IEEE Trans. Geosci. Remote Sens.*, vol. 43, no. 10, pp. 2315–2324, Oct. 2005.

[13] R. Romeiser and H. Runge, "Theoretical evaluation of several possible along-track InSAR modes of TerraSAR-X for ocean current measurements," *IEEE Trans. Geosci. Remote Sens.*, vol. 45, no. 1, pp. 21–35, Jan. 2007.

[14] R. Romeiser, S. Suchandt, H. Runge, U. Steinbrecher, and S. Gruenler, "First analysis of TerraSAR-X along-track InSAR-Derived current fields," *IEEE Trans. Geosci. Remote Sens.*, vol. 48, no. 2, pp. 820–829, Feb. 2010.

[15] R. Shuchman, "The feasibility of measurement of ocean current detection using SAR data," in *Proc. 13th Int. Symp. Remote Sens. Environ.*, 1979, pp. 93–103.

[16] B. Chapron, F. Collard, and V. Kerbaol, "Satellite synthetic aperture radar sea surface Doppler measurements," in *Proc. 2nd Workshop Coastal Marine Appl. SAR*, H. Lacoste, Ed., Sep. 2003, pp. 133–141, European Space Agency. ESA Publications Division.

[17] B. Chapron, F. Collard, and F. Ardhuin, "Direct measurements of ocean surface velocity from space: Interpretation and validation," *J. Geophys. Res.—Oceans*, vol. 110, no. C7, p. C07008, Jul. 2005.

[18] J. A. Johannessen, B. Chapron, F. Collard, V. Kudryavtsev, A. Mouche, D. Akimov, and K. Dagestad, "Direct ocean surface velocity measurements from space: Improved quantitative interpretation of Envisat ASAR observations," *Geophys. Res. Lett.*, vol. 35, no. 22, p. L22608, Nov. 2008.

[19] M. J. Rouault, A. Mouche, F. Collard, J. A. Johannessen, and B. Chapron, "Mapping the Agulhas current from Space: An assessment of ASAR surface current velocities," *J. Geophys. Res.*, vol. 115, p. C10026, Oct. 2010.

[20] W. R. Alpers, D. B. Ross, and C. L. Rufenach, "On the detectability of ocean surface-waves by real and synthetic aperture radar," *J. Geophys. Res.—Oceans Atmos.*, vol. 86, no. C7, pp. 6481–6498, 1981.

[21] V. N. Kudryavtsev, D. Hauser, G. Caudal, and B. Chapron, "A semiempirical model of the normalized radar cross section of the sea surface, 2. Radar modulation transfer function," *J. Geophys. Res.—Oceans*, vol. 108, no. C3, p. 8055, Jan. 2003.

[22] V. N. Kudryavtsev, D. Akimov, J. A. Johannessen, and B. Chapron, "On radar imaging of current features: 1. Model and comparison with observations," *J. Geophys. Res.—Oceans*, vol. 110, no. C7, p. C07016, Jul. 22, 2005.

[23] I. G. Cumming and F. H. Wong, *Digital Processing of Synthetic Aperture Radar Data: Algorithms and Implementation*. Norwood, MA: Artech House, 2005.

[24] S. N. Madsen, "Estimating the Doppler centroid of SAR data," *IEEE Trans. Aerosp. Electron. Syst.*, vol. 25, no. 2, pp. 134–140, Mar. 1989.

[25] M. Y. Jin, "Optimal range and Doppler centroid estimation for a ScanSAR system," *IEEE Trans. Geosci. Remote Sens.*, vol. 34, no. 2, pp. 479–488, Mar. 1996.

[26] R. K. Raney, "Doppler properties of radars in circular orbits," *Int. J. Remote Sens.*, vol. 7, no. 9, pp. 1153–1162, Sep. 1986.

[27] J. C. Curlander and R. N. McDonough, *Synthetic Aperture Radar—Systems and Signal Processing*. Hoboken, NJ: Wiley, 1991, ser. Remote Sensing.

[28] F. K. Li, D. N. Held, J. C. Curlander, and C. Wu, "Doppler parameter estimation for spaceborne synthetic-aperture radars," *IEEE Trans. Geosci. Remote Sens.*, vol. GE-23, no. 1, pp. 47–56, Jan. 1985.

[29] "Envisat ASAR Monthly Report March 2010," European Space Agency, 2010, Tech. Rep..

[30] A. A. Mouche, B. Chapron, N. Reul, and F. Collard, "Predicted Doppler shifts induced by ocean surface wave displacements using asymptotic electromagnetic wave scattering theories," *Waves Random Complex Media*, vol. 18, no. 1, pp. 185–196, 2008.

[31] F. Collard, A. Mouche, B. Chapron, C. Danilo, and J. A. Johannessen, "Routine high resolution observation of selected major surface currents from space," in *Proc. SeaSAR*, Frascati, Italy, 2008.

[32] A. A. Mouche, K.-F. Dagestad *et al.*, "On the use of Doppler for sea surface wind retrieval from SAR," *IEEE Trans. Geosci. Remote Sens.*, 2010, Submitted for publication.

[33] A. Stoffelen and D. Anderson, "Scatterometer data interpretation: Estimation and validation of the transfer function CMOD4," *J. Geophys. Res.—Oceans*, vol. 102, no. C3, pp. 5767–5780, Mar. 15, 1997.

[34] K. F. Dagestad, A. Mouche, F. Collard, M. W. Hansen, and J. A. Johannessen, "On the use of Doppler shift for SAR wind retrieval," in *Proc. 3rd Int. Workshop SeaSAR*, 2010, pp. 1–8.

Morten Wergeland Hansen received the Cand. Scient. degree in astrophysics from the University of Oslo, Oslo, Norway, in 2004 and an M.Sc. degree in space studies from the International Space University, Strasbourg, France, in 2006.

He has been with the Nansen Environmental and Remote Sensing Center, Bergen, Norway, since 2007 as a Research Assistant and later as a Ph.D. candidate with focus on the development and utilization of the Doppler velocity product from Envisat ASAR.

Fabrice Collard received the M.S. degree from the Ecole Centrale de Lyon, Ecully, France, in 1996, where he studied off-shore engineering, and the Ph.D. degree in oceanography and meteorology from Paris 6 University, Paris, France, in 2000. His thesis was dedicated to the 3-D aspect of wind-wave field.

He was with the Rosenstiel School of Marine and Atmospheric Science, University of Miami, Miami, where he spent two years working on HF radars as a Postdoctoral Research Associate. He is currently the Head of the R&D Department, Radar Applications Division, Collecte Localisation Satellites, Plouzané, France, working on the development and validation of surface wind, wave, and current retrieval from synthetic aperture radar.

Knut-Frode Dagestad received the Cand. Scient. degree and the Dr. Scient. degree from the University of Bergen, Bergen, Norway, in 2000 and 2005, respectively. His thesis work was performed at the Geophysical Institute, University of Bergen, in the field of atmospheric radiative transfer with application to solar energy.

Since 2005, he has been with the Nansen Environmental and Remote Sensing Center, Bergen, where he has been working on remote sensing. His main research interest is the retrieval of wind, waves, and currents from remote sensing data, with focus on synthetic aperture radar.

Johnny A. Johannessen received the Dr. Philos. degree from the University of Bergen, Bergen, Norway, in 1997.

He is currently the Vice Director of the Nansen Environmental and Remote Sensing Center, Bergen. He is also with the Geophysical Institute, University of Bergen. His experience in satellite remote sensing in oceanography and sea ice research is broad and comprehensive. In particular, he has focused on the use of synthetic aperture radar imaging capabilities to advance the understanding of mesoscale processes along the marginal ice zone and in vicinity of ocean fronts and eddies. In the last ten years, he has also been involved in the development and implementation of operational oceanography and marine forecasting both at national and international levels.

Pierre Fabry received the Ph.D. degree in signal image and speech processing from the Institut National Polytechnique de Grenoble, Grenoble, France, on the subject of blind source separation.

He spent seven years on space system engineering and radar payloads at the European Space Research and Technology Centre, European Space Agency. He joined the Division of Radar Applications, Collecte Localisation Satellites, Plouzané, France, in September 2009 and participates to the validation of the Doppler centroid products delivered on synthetic aperture radar (SAR) Level 1 data and the implementation of the new Doppler centroid estimators for future SAR products (Sentinel 1).

Bertrand Chapron received the B.Eng. degree from the Institut National Polytechnique de Grenoble, Grenoble, France, in 1984 and the Ph.D. degree in physics (fluid mechanics) from the University of Aix-Marseille II, Marseille, France, in 1988.

He was with the NASA Goddard Space Flight Center Wallops Flight Facility, Wallops Island, VA, for three years as a Postdoctoral Research Associate. He is currently a Research Scientist and the Head of the Spatial Oceanography Group, Laboratoire d'Océanographie Spatiale, Institut Français de Recherche Pour l'Exploitation de la Mer, Plouzané, France, where he is responsible for the Centre ERS Archivage et Traitement. He has been a Coinvestigator and a Principal Investigator in several projects of the European Space Agency (e.g., ENVISAT and Global Navigation Satellite System), NASA, and Centre National d'Études Spatiales (e.g., TOPEX/POSEIDON and JASON). He was also responsible (with H. Johnsen of NORUT) for the ENVISAT ASAR-wave mode algorithms and scientific preparation for the ENVISAT wind and wave products. He has experience in applied mathematics, physical oceanography, and electromagnetic wave theory and its application to ocean remote sensing.